OPEN

Correspondence and
requests for materials
should be addressed to
H.J. (hcju@inha.ac.kr)

Effects of porous properties on cold-start behavior of polymer electrolyte fuel cells from sub-zero to normal operating temperatures

Geonhui Gwak, Johan Ko & Hyunchul Ju

Department of Mechanical Engineering, Inha University, 100 Inha-ro, Nam-Gu Incheon 402-751, Republic of Korea.

In this investigation, a parametric study was performed using the transient cold-start model presented in our previous paper, in which the ice melting process and additional constitutive relations were newly included for transient cold-start simulations of polymer electrolyte fuel cells (PEFCs) from a sub-zero temperature ($-20°C$) to a normal operating temperature ($80°C$). The focus is placed on exploring the transient cold-start behavior of a PEFC for different porous properties of the catalyst layer (CL) and gas diffusion layer (GDL). This work elucidates the detailed effects of these properties on key cold-start phenomena such as ice freezing/melting and membrane hydration/dehydration processes. In particular, the simulation results highlight that designing a cathode CL with a high ionomer fraction helps to retard the rate of ice growth whereas a high ionomer fraction in the anode CL is not effective to mitigate the anode dry-out and membrane dehydration issues during PEFC cold-start.

D uring the start-up of a polymer electrolyte fuel cell (PEFC) from sub-zero to normal operating temperatures, the PEFC undergoes various cold-start stages characterizing different physiochemical, transport, and thermal processes, in which ice freezing/melting, membrane hydration/dehydration, and latent heat release/absorption processes are closely related[1–6]. It is evident that these processes and their evolution characteristics during a cold-start cycle strongly affect the performance and durability of PEFCs. Therefore, developing a full understanding of complex and interacting cold-start phenomena is essential to establish optimal cell design and operating conditions and so improve the cold-start capability of PEFCs. This is an objective where cold-start PEFC models play an important role.

A number of cold-start PEFC models have been developed and presented in the literature[7–11] in the last decade. Most of these models focused on predicting the amount of ice accumulated in the cathode catalyst layer (CL) and the resultant deterioration in cell performance, and this focus limited their simulations to narrow temperature ranges below $0°C$. Consequently, several key phenomena occurring beyond $0°C$ such as ice melting, membrane hydration/dehydration, and their strong interaction with increasing temperature were not addressed in these cold-start analyses.

In our previous study[12], we numerically explored how cold-start operating conditions affect the transient responses of PEFCs from sub-zero to normal operating temperatures. The simulation results clearly showed significant effects of these parameters on levels of ice accumulation and membrane dehydration as well as on the evolution characteristics of ice, water content, and cell temperature. The present study is an extension of our previous work[12], aiming to numerically investigate the effects of key design parameters of a membrane electrode assembly (MEA), such as ionomer fraction and porosity in the cathode CL and the porosity of GDL. This study provides a guideline for the design and optimization of MEA components to mitigate the levels of ice accumulation and membrane dehydration, and to finally enable the achievement of successful start-ups of PEFCs from sub-zero temperatures.

Results

To investigate the effects of MEA properties on the cold-start behavior of a PEFC, as shown in Table 1, we defined seven simulation cases using different ionomer fractions and porosity values for CL and GDL, which implies that the solid fraction of cathode CL, i.e. comprising carbon support and Pt particles, was accordingly adjusted by the

Table 1 | Simulation cases

Cases	Cathode				Anode				Note
	ε_i	ε_{cCL}	ε_{cGDL}	δ_{cCL} (μm)	ε_i	ε_{cCL}	ε_{cGDL}	δ_{cCL} (μm)	
Case 1	0.2	0.4	0.6	10.0	0.2	0.4	0.6	10.0	baseline
Case 2	0.3	0.3	0.6	10.0	0.2	0.4	0.6	10.0	Cathode
Case 3	0.2	0.3	0.6	10.0	0.2	0.4	0.6	10.0	
Case 4	0.3	0.4	0.6	10.0	0.2	0.4	0.6	10.0	
Case 5	0.2	0.4	0.8	10.0	0.2	0.4	0.6	10.0	
Case 6	0.2	0.4	0.6	10.0	0.3	0.3	0.6	10.0	Anode
Case 7	0.3	0.3	0.6	10.0	0.3	0.3	0.6	10.0	

changes in pore volume and ionomer fractions. As shown in Table 2, the same value of ORR kinetic parameter ($aj_{0,c}^{ref} = 10^4$ A·m^{-3}) was employed for all seven cases, meaning that Pt loading in the solid phase of the cathode CL still remains the same for Cases 1–7. In addition, the current density was 0.1 A·cm^{-2} and the initial water content in the electrolyte phase was assumed to be 10 for all simulation cases.

Figure 1 shows the average cell temperature and voltage evolution curves in the cathode CL for Cases 1–5. First, the rates of cell temperature rise for five simulation cases are almost identical to each other, which imply that the amounts of waste heat released in all five cases are also similar. Accordingly, cell voltages in all five cases remain at almost the same level, indicating similar reversible/irreversible voltage losses for Cases 1–5. The slightly higher cell performances achieved in Cases 2 and 4 at the latter cold-start stages (after 400 s) are mainly due to their higher ionomer fractions in the cathode CL (i.e., 0.3) and resultant lower ohmic voltage losses for proton transport through the cathode CL.

Figure 2 shows the evolution profiles of cumulative ice mass in the cathode CL. The ice accumulation curves for Cases 1–5 exhibit three distinct stages representing freezing, no desublimation, and melting. Firstly, it is seen that using a higher ionomer fraction in the cathode CL prolongs the time at which the ice formation begins owing to an increase in the water uptake capacity of the cathode CL. For instance, as the ionomer fraction in the cathode CL is raised from 0.2 to 0.3 for the same CL porosity of 0.4 (Case 1 vs. Case 4), the time at which ice appears is delayed from 1.6 s to 4.4 s. Secondly, the porosity of the cathode CL mainly controls the rate of ice growth inside a cell.

Comparison of Case 1 with Case 3 or Case 2 with Case 4 clearly indicates that the higher CL porosity results in a slower ice growth rate because of the larger vapor storage capacity in the cathode CL. Consequently, among Cases 1–5, Case 4 exhibits the lowest amount of cumulative ice mass due to a combined result of its higher ionomer fraction and larger porosity at the cathode CL. Specifically, the maximum ice mass in Case 4 is approximately 0.095 mg·cm^{-2}, whereas the highest ice accumulation, 0.323 mg·cm^{-2}, is predicted in Case 3 due to its lower ionomer fraction and porosity. Finally, an increase in the cathode GDL porosity slightly lowers the amount of ice in the cathode CL, which is mainly caused by enhanced vapor phase diffusion via an increase of the effective diffusivity of water vapor. The enhanced vapor phase diffusion with higher GDL porosity can be confirmed by comparing the cumulative ice mass evaluation curves in the cathode GDL between Cases 1 and 5 in Figure 3; Here, even if the total cumulative ice mass for both Cases 1 and 5 are practically equivalent, the specific ice mass in the cathode GDL increases from 0.072 (Case 1) to 0.083 mg·cm^{-2} (Case 5) with increasing GDL porosity from 0.6 to 0.8.

Figure 4 displays the water content evolution curves corresponding to the anode and cathode CLs, and to the membrane regions for Cases 1–5. In the very early cold-start stages within 4.8 s, some severe anode dehydration is seen for all five cases; the water content in the anode CL and in the membrane drops from the initial value (i.e., 10) to the level of 3.67–3.69, implying that the EOD flux dominates over the water back-flow because of the very low water diffusion coefficient through the membrane at sub-zero temperatures (i.e., at the anode dehydration stage). In contrast, the water content of the cathode CL increases and quickly reaches saturation (i.e., 14) due to water production by ORR. After the anode dehydration stage, a second dehydration occurs mainly in the cathode CL while the decreases in water content in the anode CL and in the membrane are almost equivalent. Therefore, the cathode dehydration stage can be defined as that period for which the rate of increase of vapor saturation pressure (driven by the increasing cell temperature) is dominant over the rate of water production by the ORR.

The dehydrated cathode CL is then suddenly hydrated in the time range 89.2–104.5 s, which is indicative of ice melting. According to Figures 1 and 2, it is clear that the water content surge period for each case corresponds to the ice-melting period near 0°C. In addition, the magnitude of the sudden sharp increase in the water content of the

Table 2 | Physiochemical parameters and component properties

| Description	Value
Exchange current density × Ratio of reaction surface to CL volume in the anode side ($ai_{0,a}^{ref}$)[22]	1.0×10^9 A m^{-3}
Exchange current density × Ratio of reaction surface to CL volume in the cathode side ($ai_{0,c}^{ref}$)[14]	1.0×10^4 A m^{-3}
Reference hydrogen molar concentration (C_{H2}^{ref})[22]	40.88 mol m^{-3}
Reference oxygen molar concentration (C_{O2}^{ref})[22]	40.88 mol m^{-3}
Anodic and cathodic transfer coefficients for hydrogen oxidation reaction	$\alpha_a + \alpha_c = 2$
Cathodic transfer coefficient for oxygen reduction reaction	$\alpha_c = 1$
Dry membrane density (ρ^{mem})[23]	1980 kg m^{-3}
Equivalent weight of electrolyte in the membrane (EW)[24]	1.1 kg mol^{-1}
Faraday constant (F)	96487 C mol^{-1}
Universal gas constant (R)	8.314 J mol^{-1} K^{-1}
Porosity of the GDL/CL ($\varepsilon_{GDLs}/\varepsilon_{CLs}$)	0.6/0.4
Volume fraction of ionomer in CLs (ε_I)	0.2
Permeability of the GDL/CL (K_{GDLs}/K_{CLs})[20]	$1 \times 10^{-12}/1 \times 10^{-13}$ m^2
Effective electronic conductivity in GDL/CL ($\sigma_{GDLs}/\sigma_{CLs}$)[20]	300/300 S m^{-1}
Effective electronic conductivity in metal bipolar plate (σ_{mBP})[14]	1×10^6 S m^{-1}
Thermal conductivity of GDL/CL (k_{GDLs}/k_{CLs})[20]	1.5/1.2 W m^{-1} K^{-1}
Thermal conductivity of membrane (k_{mem})[20]	0.95 W m^{-1} K^{-1}
Thermal conductivity of metal bipolar plate (k_{mBP})[14,25]	13.4 W m^{-1} K^{-1}
Heat capacity of GDL/CL ($\rho C_{p,GDLs}/\rho C_{p,CLs}$)[14]	568/3300 kJ m^{-3} K^{-1}
Heat capacity of membrane ($\rho C_{p,mem}$)[20,25]	1650 kJ m^{-3} K^{-1}
Heat capacity of metal bipolar plate ($\rho C_{p,mbp}$)[14]	7703 kJ m^{-3} K^{-1}
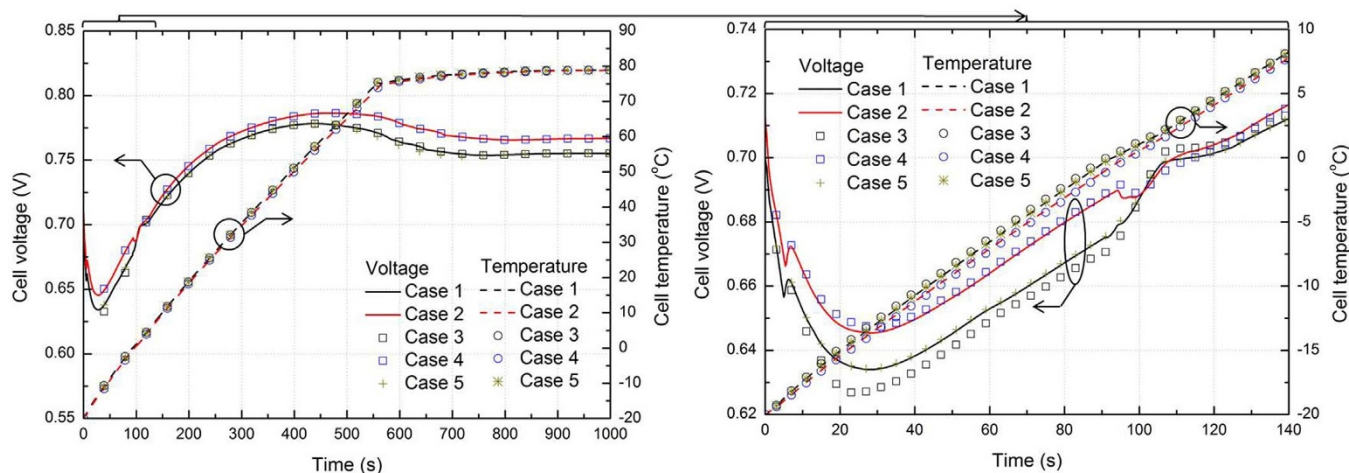
Figure 1 | Cell voltage and temperature evolution curves for Cases 1–5.

cathode CL is proportional to the ice accumulation level to be melted. For instance, Case 3 has the largest amount of ice melting among Cases 1–5 and therefore the highest increase in the water content. After the ice melting stage, the anode and cathode CLs as well as the membrane are slowly dehydrated due to a continuous cell temperature increase during the cold-start process. In addition, it is seen that the water content gradient between the cathode and anode CLs becomes smaller at the latter cold-start stages because of the enhanced water back-flow by increasing cell temperature.

To address the effects of ionomer fraction and porosity in the anode CL, Figures 5 and 6 compare cell temperature and voltage changes for Cases 1, 6, and 7 and their evolution profiles of cumulative ice mass, respectively. First, it is seen that the cell performance in the early cold-start stages (during the first 40 s) is improved, when the higher ionomer fraction (i.e., 0.3) and lower porosity (i.e., 0.3) are employed for the anode CL (Cases 6 and 7). Figure 7 displays the water content contours in the anode/cathode CLs and in the membrane at 30 s for Cases 1, 6, and 7. Although slightly higher electrolyte hydration is achieved in Cases 6 and 7, a distinct difference between the cases is not observed. Therefore, the higher cell perform-

ance in Cases 6 and 7 compared with that of Case 1 (see Figure 5) is mainly due to improved effective proton conductivity by using a higher ionomer fraction for the anode CL (see Eq. (20)).

When the cumulative ice mass curves for Cases 6 and 7 are compared with that of Case 1 in Figure 6, Case 6 exhibits slightly higher ice accumulation, whereas the ice accumulation level is lower in Case 7. The higher ice accumulation in Case 6 results from a smaller water gradient from the cathode to the anode driven by the higher ionomer fraction and lower porosity in the anode CL, which reduces the water back-flow from the cathode to the anode. The averaged water content profiles in the anode and cathode CLs and membrane in Figure 8 clearly indicate that the water content gradient of Case 6 is relatively less steep compared with that of Case 1 during the ice growth stage (the first 13 s). Therefore, in Case 6, relatively more water is frozen in the cathode CL rather than being transported towards the anode. In contrast, the lower ice accumulation in Case 7 is due to its higher water uptake potential in the cathode CL, which in turn is caused by the higher ionomer fraction (i.e., 0.3) that retards the formation of ice. As discussed in Figure 5, the higher cell voltage achieved in Case 7 compared with Case 6 is due mainly to its lower proton transport
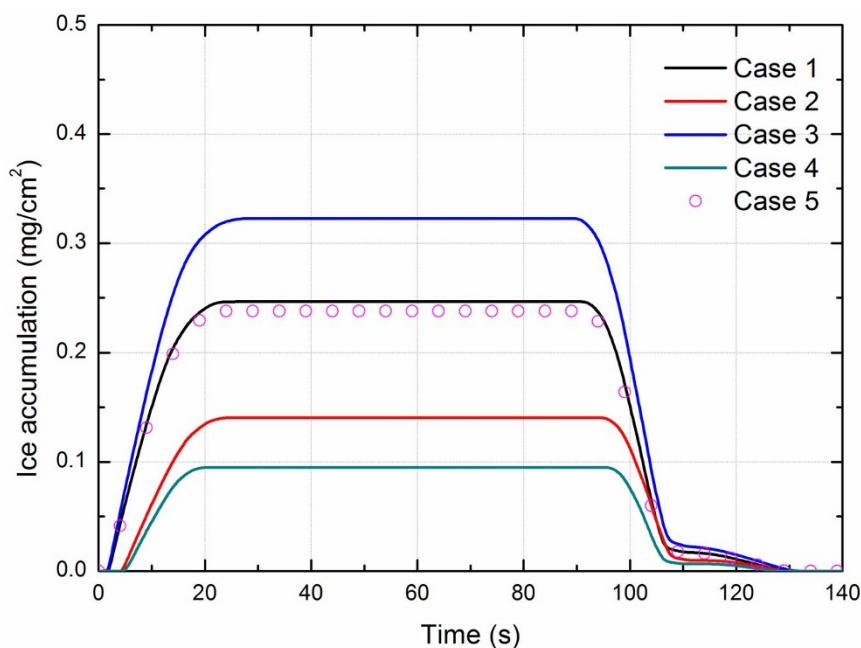

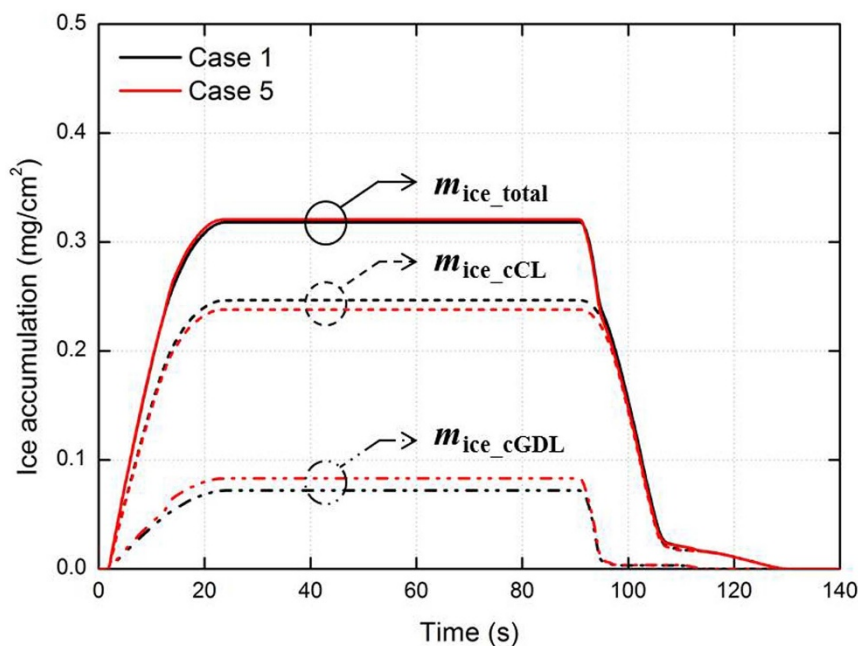**Figure 2 | Ice accumulation evolution curves in the cathode CL for Cases 1–5.**

Figure 3 | Ice accumulation evolution curves in the cathodes GDL, CL, and the total ice accumulation curves for Cases 1 and 5.

resistance through the cathode CL. More importantly, it can be observed in Figure 8 that the water content curves of anode CL corresponding to Cases 1 and 6 are almost identical to each other throughout the entire cold-start period. This fact indicates that the anode dry-out issue during cold-start is not successfully mitigated by using the higher ionomer fraction for the anode CL.

Discussion

Using the transient cold-start PEFC model, we carried out a parametric study to analyze the influence of porous properties of GDL and CL on the cold-start behavior of a PEFC operating from sub-zero to normal temperatures. From the simulation results, the following specific conclusions can be drawn.

It is clearly demonstrated by transient cold-start simulations that ice formation and growth inside a cell at sub-zero temperatures are significantly influenced by the porous properties of the cathode CL and GDL. While using a higher electrolyte content for the cathode CL helps to enhance its water uptake capability, the period when vapor is

fully saturated and ice nucleation starts was successfully delayed by designing the pore volume of the cathode CL to be larger. As a result, the ice accumulation was reduced by designing a cathode CL with higher ionomer fraction and porosity. In addition, designing the cathode GDL to have larger porosity increased the vapor phase diffusion flux between the cathode CL and GDL and was thereby helpful in reducing the amount of ice in the cathode CL. In contrast to the changed ice accumulation trend at the cathode CL, neither the anode dry-out nor the membrane dehydration issues during PEFC cold-start were effectively resolved by altering the porous designs of the cathode CL and GDL, because during PEFC cold-start, those phenomena are mainly controlled by the EOD effect.

Unexpectedly, the ionomer faction of the anode CL was influential in ice accumulation in the cathode CL at the cold-start stages below $0°C$. At a large ionomer fraction at the anode CL, the water back-flow from the cathode to the anode was reduced, which led to faster ice growth at the cathode CL. As the cell temperature increased above $0°C$, its impact on the water content profiles became almost neg-
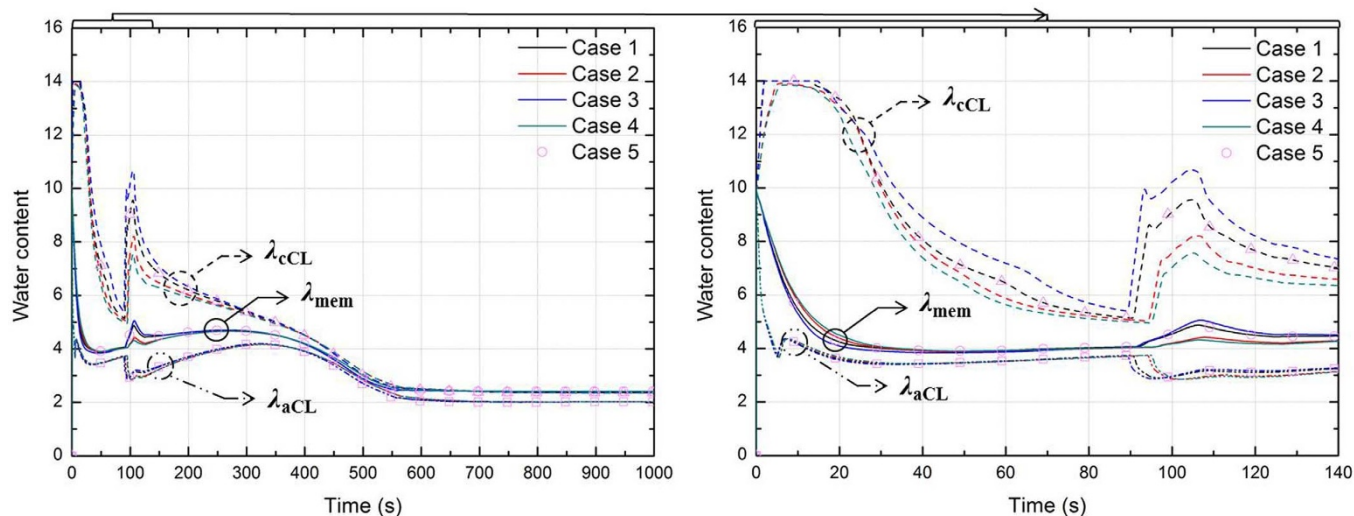

Figure 4 | Water content evolution curves for Cases 1–5; the values were averaged in the anode CL, in the cathode CL, and in the membrane, respectively.
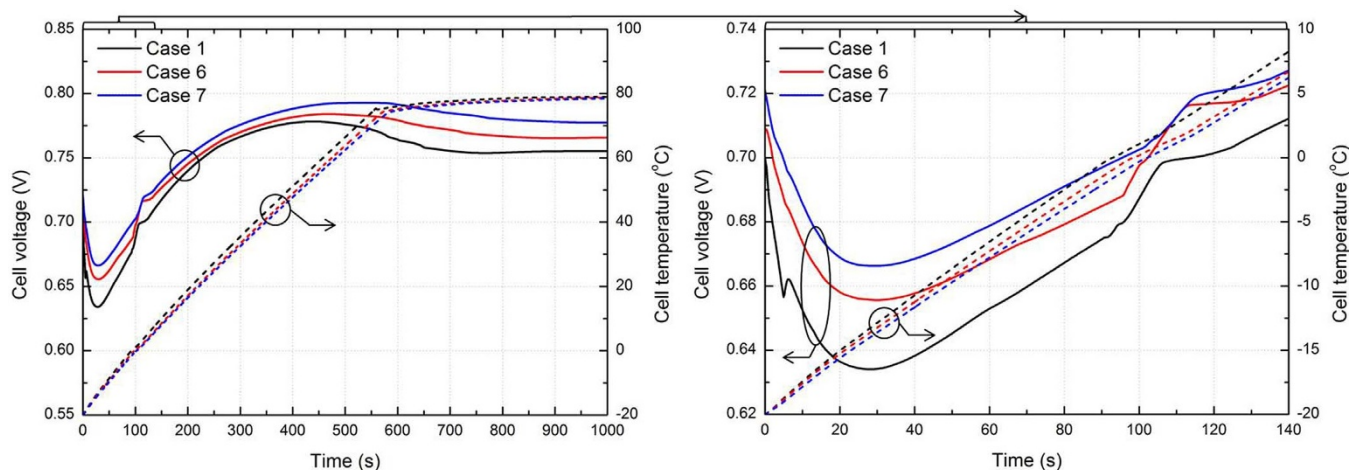
Figure 5 | Cell voltage and temperature evolution curves for Cases 1, 6, and 7.

ligible. Therefore, designing the anode CL with higher ionomer fraction is not an effective way to reduce anode dehydration problems during PEFC cold-start.

Methods

For simulation of a PEFC operating under a wide temperature range from sub-zero ($-20°C$) to normal operating temperatures ($80°C$), the three-dimensional, non-isothermal cold-start PEFC model developed in previous studies[10,13–15] was enhanced by including ice melting and constitutive relationships for PEFC transient simulation above $0°C$. A detailed description of the cold-start PEFC model has already been provided in our previous paper[10]; therefore, we present here only a brief description, with an emphasis on the new features included in this study.

Model assumptions. The specific assumptions used in the model are as follows:

(1) incompressible and laminar flow in gas channels and porous components of a PEFC as a result of small pressure gradient and flow velocities;
(2) ideal gas mixtures;
(3) a negligible gravitational effect;
(4) isotropic and homogeneous porous layers for GDLs and CLs, i.e., characterized by effective porosity and permeability;
(5) instantaneous de-sublimation of water vapor at saturation; and negligible electrochemical double-layer charging and discharging at CLs.

Governing equations and source/sink terms. Under the aforementioned assumptions, the multiphase PEFC model is governed by the conservations of mass, momentum, species, energy, and charge as follows:

Mass conservation:

$$\frac{\partial(\varepsilon_s \rho_s)}{\partial t} + \frac{\partial(\varepsilon \rho)}{\partial t} + \nabla \cdot (\rho \vec{u}) = S_m \tag{1}$$

Momentum conservation:

$$\frac{1}{\varepsilon}\left[\frac{\partial(\rho \vec{u})}{\partial t} + \frac{1}{\varepsilon}\nabla \cdot (\rho \vec{u}\vec{u})\right] = -\nabla p + \nabla \cdot \tau + \rho \vec{g} + S_u \tag{2}$$

Species conservation:

$$\frac{\partial(\varepsilon C_i)}{\partial t} + \nabla \cdot (\vec{u} C_i) = \nabla \cdot \left(D_i^{eff} \nabla C_i\right) + S_i \tag{3}$$

Energy conservation:

$$\frac{\partial(\varepsilon \rho C_p T)_{cell}}{\partial t} + \frac{\partial(\varepsilon \rho C_p T)_g}{\partial t} + \nabla \cdot (\rho C_p \vec{u} T)$$
$$= \nabla \cdot \left(k^{eff} \nabla T\right) + S_T \tag{4}$$
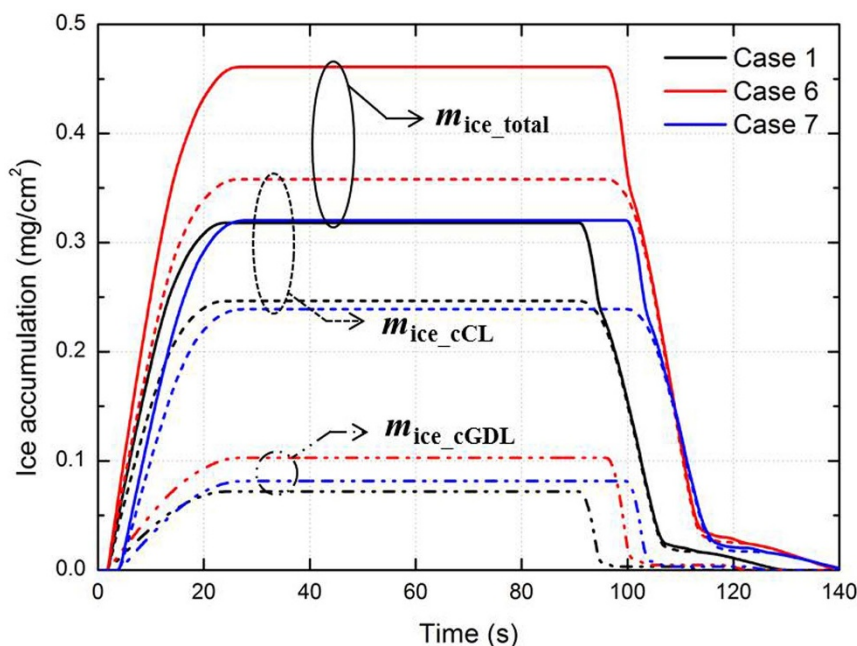
Charge conservation:

Figure 6 | Ice accumulation evolution curves in the cathode GDL, CL, and total ice accumulation curves for Cases 1, 6, and 7.
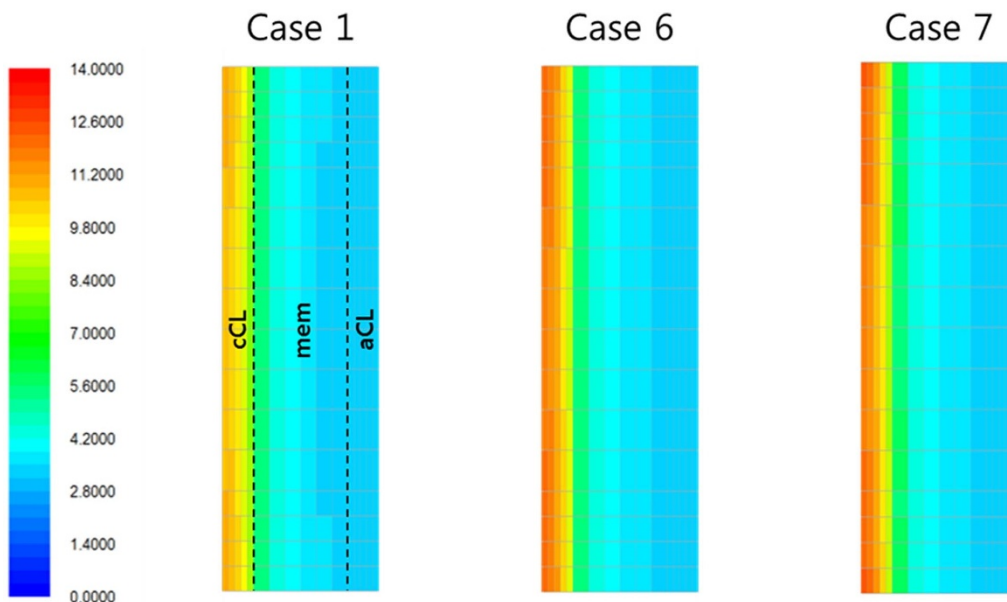
Figure 7 | Water content contours for Cases 1, 6, and 7 (at 30 s).

Proton transport:

$$\nabla \cdot \left(\kappa^{eff} \nabla \varphi_e \right) + S_\varphi = 0 \tag{5}$$

Electron transport:

$$\nabla \cdot \left(\sigma^{eff} \nabla \varphi_s \right) - S_\varphi = 0 \tag{6}$$

The source/sink terms in the conservation Eqs. (1)–(6), i.e., S_m, S_u, S_i, S_T, and S_Φ, are listed in Table 3. Note that the source terms, S_i, in the water transport equations for the CL and GDL regions include a phase-change term, S_{sg}, to describe ice formation, growth, and melting processes during a cold-start. The detailed description of S_{sg} is as follows:

$$S_{sg} = \begin{cases} 0 & \text{when } C_{H_2O} \leq C_{H_2O}^{sat} \\ R_{desub}\left(C_{H_2O}^{sat} - C_{H_2O}\right) & \text{when } C_{H_2O} > C_{H_2O}^{sat} \ \& \ T < T_{freeze}^{H_2O} \\ R_{sub}\left(C_{H_2O}^{sat} - C_{H_2O}\right) & \text{when } T = T_{freeze}^{H_2O} \ \& \ s > 0 \\ 0 & \text{when } T \geq T_{freeze}^{H_2O} \ \& \ s = 0 \end{cases} \tag{7}$$

where R_{desub} and R_{sub} are the phase-change rates for desublimation and sublimation, respectively, and s denotes the ice fraction, defined as the volume fraction of the ice to the void spaces in porous media such as the GDL and CL, i.e.,

$$s = \frac{V_{ice}}{V_{void}} \tag{8}$$

Therefore, the amount of ice accumulated in the PEFC components is described in terms of the ice fraction, s. The desublimation and sublimation processes lead to latent heat release and absorption; therefore, these effects should be considered in the source terms, S_T, in the energy conservation equation for the CL and GDL regions, i.e., $h_{sg} \cdot S_{sg}$ in Table 3.

The source terms, S_Φ, for the charge conservation equations account for the hydrogen oxidation reaction (HOR) in the anode CL and the oxygen reduction reaction (ORR) in the cathode CL. These electrochemical reactions are represented by linearizing the standard Butler–Volmer equation for the HOR, and by neglecting the anodic reaction term of the Butler–Volmer equation for the ORR.

HOR in the anode CL:

$$j = a i_{0,a}^{ref} \left(\frac{C_{H_2}}{C_{H_2}^{ref}} \right)^{1/2} \left(\frac{\alpha_a + \alpha_c}{RT} F\eta \right) \tag{9}$$
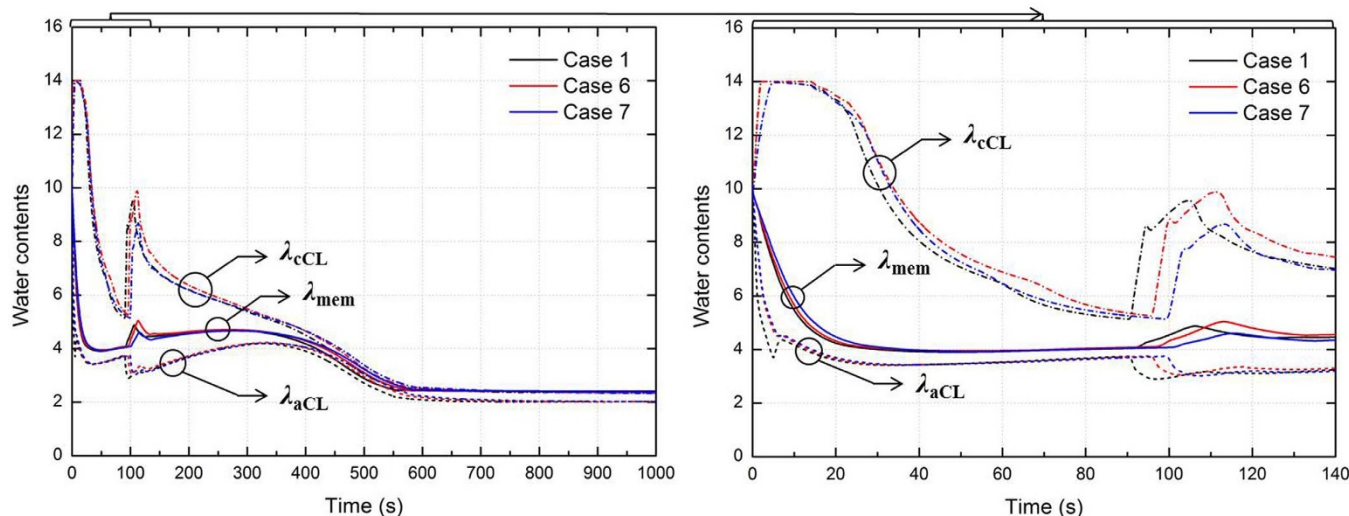

Figure 8 | Water content evolution curves for Cases 1, 6, and 7; the values were averaged in the anode CL, in the cathode CL, and in the membrane, respectively.

Table 3 | Three-dimensional transient polymer-electrolyte fuel-cell model: source/sink terms

Mass
In CLs: $S_m = MW_i \dfrac{j}{nF} + MW_{H_2O}\left[\nabla\cdot\left(D_{H_2O}^{mem}\nabla C_{H_2O}\right)-\nabla\cdot\left(n_d\dfrac{I}{F}\right)\right]$

Momentum
In GDL/CLs: $S_u = \dfrac{\mu}{K}\vec{u}$
In membrane: $\vec{u}=0$

Species
For water in CLs: $S_i = -\nabla\cdot\left(\dfrac{n_d}{F}I\right) - \dfrac{s_i j}{nF}S_{sg}$
For water in GDLs: $S_i = S_{sg}$
For order species: $S_i = -\dfrac{s_i j}{nF}$

Energy
In CLs: $S_r = j\left(\eta + T\dfrac{dU_0}{dT}\right) + \dfrac{I_e^2}{\kappa^{eff}} + \dfrac{I_s^2}{\sigma^{eff}} + h_{sg}\cdot S_{sg}$
In GDLs: $S_r = \dfrac{I_s^2}{\sigma^{eff}} + h_{sg}\cdot S_{sg}$
In membrane: $S_T = \dfrac{I_e^2}{\kappa^{eff}}$

Charge
In CLs: $S_\phi = j$

Electrochemical reactions
$\sum_k s_i M_i^z = ne^-$, where $\begin{cases} M_i = \text{chemical formula of species i} \\ s_i = \text{stoichiometry coefficient} \\ n = \text{number of electrons transferred} \end{cases}$

Hydrogen oxidation reaction (HOR) at anode side: $H_2 - 2H^+ = 2e^-$
Oxygen reduction reaction (ORR) at cathode side: $2H_2O - O_2 - 4H^+ = 4e^-$

ORR in the cathode CL:

$$j = -ai_{o,c}^{ref}(1-s)\left(\frac{C_{O_2}}{C_{O_2}^{ref}}\right)^{3/4}\exp\left(-\frac{\alpha_c}{RT}F\eta\right) \qquad (10)$$

The surface overpotentials, η, for the HOR and ORR are defined using the thermodynamic equilibrium potential, U_0, between the anode and cathode sides as follows:

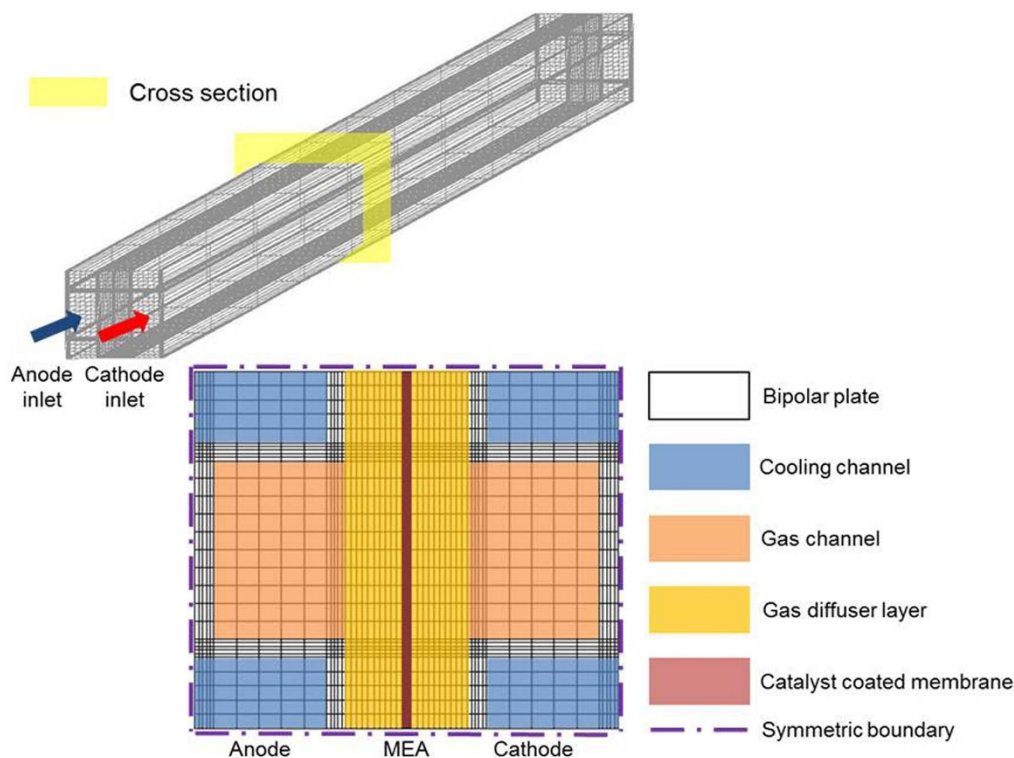$$\eta = \phi_s - \phi_e - U_0 \qquad \text{Anode:} \quad U_0 = 0 \qquad (11)$$

Cathode: $\quad U_0 = 1.23 - 9.0\times10^{-4}(T-298.15) \qquad (12)$

In the right-hand side of the species equation, Eq. (3), the effective diffusion coefficient, D_i^{eff}, is modified by the Bruggeman correlation[16] to account for the effects of the porosity and tortuosity of the GDL and CL. Because it is also affected by the ice fraction, s, the final form of D_i^{eff}, in the presence of ice becomes:

$$D_i^{eff} = [\varepsilon(1-s)]^n D_i \qquad (13)$$

The transport properties of electrolytes are correlated with the water content of the membrane, λ, which is in turn a function of the water activity, a, as follows[17]:

$$a = \frac{C_w^g R_u T}{P_{sat}} \qquad (14)$$

$$\lambda = \begin{cases} 0.043 + 17.81a - 39.85a^2 + 36.0a^3 & 0 < a \le 1 \\ 14 & a = 1 \end{cases} \quad for\ T < 273.15 \qquad (15)$$

$$\lambda = \begin{cases} 0.043 + 17.81a - 39.85a^2 + 36.0a^3 & 0 < a \le 1 \\ 14 + 1.4(a-1) & 1 \le a \le 3 \\ 16.8 & 3 < a \end{cases} \quad for\ T \ge 273.15 \qquad (16)$$

The water vapor partial pressure can be calculated over a wide temperature range from sub-zero to normal temperatures as follows[17,18]:

$$\log_{10} P_{sat} = -9.09718\times(273.16/T - 1) - 3.56654$$
$$\log_{10}\left(\frac{273.16}{T}\right) + 0.876793(1-T/273.16) \qquad (17)$$
$$+ \log_{10} 6.1071 + 2 \quad for\ T < 279.15$$

$$\log_{10} P_{sat} = -2.1794 + 0.02953(T-273.15)$$
$$-3.1837\times10^{-5}(T-273.15)^2$$
$$+1.4454\times10^{-7}(T-273.15)^3 \qquad (18)$$
$$for\ T \ge 279.15$$

The EOD coefficient, n_d, and the proton conductivity in the membrane, κ, have been reported by Zawodzinsky et al.[19], and Mao et al.[20], respectively. And the expression for

Figure 9 | Configuration of computational domain and mesh with boundary conditions for single straight-channel fuel-cell geometry.

Table 4	Cell dimensions and operating conditions	
Description	Value
Cell length	0.1 m
Anode/cathode channel/rib width	1.0×10^{-3} m
Anode/cathode channel height	0.7×10^{-3} m
Thickness of anode/cathode GDLs (δ_{GDLs})	300×10^{-6} m
Thickness of anode/cathode CLs (δ_{CLs})	10×10^{-6} m
Thickness of membrane (δ_{mem})	30×10^{-6} m
Anode/cathode pressure (P)	1/1 atm
Anode/cathode stoichiometry (ζ_a/ζ_c)	1.5/2.0
Anode/cathode inlet temperature	$-20°C$
Operating current density (I)	1000 A m^{-2}
Startup temperature	$-20°C$
Water content (λ)	10.0
Relative humidity	0.0/0.0

the water diffusion coefficient in the membrane, D_w^{mem}, has been given by Motupally et al.[21].

$$n_d = \begin{cases} 1 & for \ \lambda \leq 14 \\ \frac{1.5}{8} \times (\lambda - 14) + 1 & otherwise \end{cases} \quad (19)$$

$$\kappa = (0.5139\lambda - 0.326) \exp\left[2222\left(\frac{1}{303} - \frac{1}{T}\right)\right] \quad (20)$$

$$D_w^{mem} = \begin{cases} 3.10 \times 10^{-3}\lambda\left(-1 + e^{0.28\lambda}\right)e^{\left(\frac{-2436}{T}\right)} & for \ 0 < \lambda \leq 3 \\ 4.17 \times 10^{-4}\left(1 + 161e^{-\lambda}\right)e^{\left(\frac{-2436}{T}\right)} & for \ 3 \leq \lambda < 17 \end{cases} \quad (21)$$

Boundary conditions and numerical implementation. The cell geometry and its computational mesh for the present study are shown in Figure 9. The detailed physiochemical parameters, cell dimensions, operating conditions, and material properties are listed in Tables 2 and 4.

The anode/cathode inlet velocities can be determined from their respective stoichiometric ratios (ζ_a and ζ_c) and the operating current density (I) as follows:

$$\text{Anode inlet}: \ \vec{u}_{in,a} = \frac{\zeta_a \frac{I}{2F} A_{act}}{C_{H_2} A_{a,chan}} \quad (22)$$

$$\text{Cathode inlet}: \ \vec{u}_{in,c} = \frac{\zeta_c \frac{I}{4F} A_{act}}{C_{O_2} A_{c,chan}} \quad (23)$$

where $A_{a,chan}$ and $A_{c,chan}$ represent the inlet cross-sectional areas of the anode and cathode gas channels, respectively. The inlet molar concentrations of hydrogen and oxygen (C_{H_2} and C_{O_2}) can be calculated from the inlet pressure, humidification condition, and temperature, according to the ideal gas law.

The transient cold-start model were numerically implemented with a commercially available computational fluid dynamics program, FLUENT version 14.5, using FLUENT's user-defined functions. The convergence criteria for all species and energy residuals were set to 10^{-7}.

1. Ciureanu, M. Effects of Nafion dehydration in PEM fuel cells. *J Applied Electrochem* **34**, 705–714 (2004).
2. Hou, J. *et al.* Investigation of resided water effects on PEM fuel cell after cold start. *Int J Hydrogen Energy* **32**, 4503–4509 (2007).
3. Chacko, C. *et al.* Characteristic behavior of polymer electrolyte fuel cell resistance during cold start. *J Electrochem Soc* **155**, B1145–1154 (2008).
4. Alink, R., Gerteisen, D. & Oszcipok, M. Degradation effects in polymer electrolyte membrane fuel cell stacks by sub-zero operation-An in situ and ex situ analysis. *J Power Sources* **182**, 175–187 (2008).
5. Dursch, T. J. *et al.* Non-isothermal melting of ice in the gas-diffusion layer of a proton-exchange-membrane fuel cell. *Int J Heat and Mass Transfer* **67**, 896–901 (2013).
6. Jiao, K. & Li, X. Three-dimensional multiphase modeling of cold start processes in polymer electrolyte membrane fuel cells. *Electrochim Acta* **54**, 6876–6891 (2009).
7. Mao, L. & Wang, C. Y. Analysis of cold start in polymer electrolyte fuel cells. *J Electrochem Soc* **154**, B139–146 (2007).
8. Meng, H. A PEM fuel cell model for cold-start simulations. *J Power Sources* **178**, 141–150 (2008).
9. Kinha, P. K. & Wang, C. Y. Two-phase modeling of gas purge in a polymer electrolyte fuel cell. *J Power Sources* **183**, 609–618 (2008).
10. Ko, J. H. & Ju, H. C. Comparison of numerical simulation results and experimental data during cold-start of polymer electrolyte fuel cells. *Appl Energ* **94**, 364–374 (2012).
11. Wang, Y. *et al.* Cold start of polymer electrolyte fuel cells: Three-stage startup characterization. *Electrochim Acta* **55**, 2636–2644 (2010).
12. Geonhui, G. H., Ko, J. H. & Ju, H. C. Numerical investigation of cold-start behavior of polymer-electrolyte fuel-cells from subzero to normal operating temperatures – Part I: Effects of cell boundary and operating conditions. *Int J Hydrogen Energy* in press (2014).
13. Ko, J. H. & Ju, H. C. Effects of cathode catalyst layer design parameters on cold start behavior of polymer electrolyte fuel cell (PEFCs). *Int J Hydrogen Energy* **38**, 682–691 (2013).
14. Ko, J. H. *et al.* Impact of metallic bipolar plates on cold-start behaviors of Polymer Electrolyte Fuel Cells (PEFCs). *Solid State Ionics* **225**, 260–267 (2012).
15. Ko, J. H., Kim, W. G., Lim, Y. D. & Ju, H. C. Improving the cold-start capability of polymer electrolyte fuel cells (PEFCs) by using a dual-function micro-porous layer (MPL): Numerical simulations. *Int J Hydrogen Energy* **38**, 652–659 (2013).
16. Meredith, R. E. & Tobias, C. W. *Advances in Electrochemistry and Electrochemical Engineering* (Interscience publishers, 1962).
17. Springer, T. E., Zawodinski, A. & Gottesfield, S. Polymer electrolyte fuel cell model. *J Electrochem Soc* **138**, 2334–2342 (1991).
18. Murphy, D. M. & Koop, T. Review of the vapour pressures of ice and supercooled water for atmospheric applications. *Q J R Meteorol Soc* **131**, 1539–1565 (2005).
19. Zawodzinski, T. A. *et al.* Water uptake by and transport through Nafion 117 membranes. *J Electrochem Soc* **140**, 1041–1047 (1993).
20. Mao, L., Wang, C. Y. & Tabuchi, Y. A multiphase model for cold start of polymer electrolyte fuel cells. *J Electrochem Soc* **154**, B341–351 (2007).
21. Motupally, S., Becker, A. J. & Weidner, J. W. Diffusion of water in Nafion 115 membranes. *J Electrochem Soc* **147**, 3171–3177 (2000).
22. Ju, H., Wang, C. Y., Cleghorn, S. & Beuscher, U. Nonisothermal modeling of polymer electrolyte fuel cells: I. Experimental validation. *J Electrochem Soc* **152**, A1645–1653 (2005).
23. Kim, D. S., Kim, Y. S., Michael, D. G. & Bryan, S. P. High performance nitrile copolymers for polymer electrolyte membrane fuel cells. *J Membrane Sci* **321**, 199–208 (2008).
24. Rikukawa, M. & Sanui, K. Proton conducting polymer electrolyte membranes based on hydrocarbon polymers. *Prog Polym Sci* **25**, 1463–1502 (2000).
25. Incropera, F. P. & Dewitt, D. P. *Fundamentals of Heat and Mass Transfer* (John Wiley & Sons, New York, 2002).

Author contributions

G.G. and J.K. performed cold-start coding and simulations. G.G. prepared figures 1–9 and Tables 1–4. H.J. designed and supervised the study and wrote the manuscript. All authors reviewed the manuscript.

Additional information

Competing financial interests: The authors declare no competing financial interests.

How to cite this article: Gwak, G., Ko, J. & Ju, H. Effects of porous properties on cold-start behavior of polymer electrolyte fuel cells from sub-zero to normal operating temperatures. *Sci. Rep.* **4**, 5770; DOI:10.1038/srep05770 (2014).